

Development of the calibration method for a fast steering antenna for investigating the mode conversion window used in EBW heating in the LHD plasma

メタデータ	言語: eng 出版者: 公開日: 2021-06-30 キーワード (Ja): キーワード (En): 作成者: Goto, Yuki, Kubo, Shin, Igami, Hiroe, Nishiura, Masaki, SHIMOZUMA, Takashi, Yoshimura, Yasuo, Takahashi, Hiromi, Tsujimura, Ii Toru メールアドレス: 所属:
URL	http://hdl.handle.net/10655/00012533

This work is licensed under a Creative Commons Attribution-NonCommercial-ShareAlike 3.0 International License.



Development of the Calibration Method for a Fast-steering Antenna for Investigating of the Mode Conversion Window Used in EBW Heating in the LHD Plasma

Yuki Goto^{1*}, Shin Kubo^{1,2}, Hiroe Igami², Masaki Nishiura², Takashi Shimoizuma², Yasuo Yoshimura², Hiromi Takahashi², and Toru Ii Tsujimura²

¹Department of Applied Energy, Nagoya University, Nagoya 464-8603, Japan

²National Institute for Fusion Science, National Institutes of Natural Sciences, Toki 509-5292, Japan

In this study, we developed a calibration method for a fast-steering antenna for investigating the mode conversion window used in Electron Bernstein Wave (EBW) heating in the Large Helical Device (LHD). The calibration was carried out in under-dense plasma against a line-of-sight with an optical thickness which varied spatially. Although multi-reflected background radiation becomes dominant in optically thin lines-of-sight, we succeeded in calibrating the fast-steering antenna by including the effect of multi-reflected background radiation in the solution of the radiation transfer equation as the constant by which the temperature of the center of the plasma is multiplied. In addition, we report the initial results of experiments investigating the mode conversion window in over-dense plasma using the calibrated antenna.

1. Introduction

In a fusion experimental device, it is important to generate and sustain the high electron temperature plasma by direct electron heating. Also, it is possible to improve the confinement performance by controlling the electron temperature distribution. In the Large Helical Device (LHD), Electron Cyclotron Resonance Heating (ECRH) using high-power high-frequency gyrotrons has been carried out. To date, three 1 MW gyrotrons at 77 GHz have been installed on the LHD. The power from these gyrotrons can penetrate into a plasma with density below $n_{e,\text{cut-off}} = 7.35 \times 10^{19} \text{m}^{-3}$ and heat plasma at a resonant magnetic field $B = 2.75 \text{ T}$, where $n_{e,\text{cut-off}}$ is the plasma cut-off density. When plasma density n_e is satisfied with $n_e > n_{e,\text{cut-off}}$, the plasma is called over-dense plasma. In the opposite case, the plasma is called under-dense plasma.

Since an Electron Bernstein Wave (EBW) can propagate into the plasma without a density limit and is absorbed at the resonance layer, it can be used for plasma heating and current drive in over-dense plasma.^{1–11)} Since the EBW is an electrostatic wave, EBW has to be excited through a mode conversion process by an externally injected electromagnetic wave from the vacuum side. The EBW can be excited via the OXB mode conversion process, where O, X, and B indicate the ordinary, extraordinary, and electron Bernstein waves, respectively.^{12–14)} O-mode injection is the first step of the OXB mode conversion mechanism, and the mode conversion efficiency has a narrow peak near an optimum propagating angle relative to the magnetic field at the plasma cut-off.^{5, 15)} This optimal angle is a function of the plasma parameter at the mode conversion region.^{16–18)} It is essential to tune the injection direction precisely to aim at the region where mode conversion efficiency is high. This region is called mode conversion window. A thermally excited EBW in the plasma core region can be emitted as the O-mode via the inverse OXB mode conversion mechanism (Electron Bern-

stein Emission: EBE).^{19, 20)} In the over-dense case, an electromagnetic wave cannot propagate into the plasma nor be emitted from the plasma. Therefore, an Electron Cyclotron Emission (ECE) is not measured when over-dense plasma is sustained. However, the mode converted EBE which passes through the mode conversion window can be detected. For investigation of the efficient mode conversion window, it is important to measure the ECE/EBE around the mode conversion window when over-dense plasma is sustained. For this purpose, a fast steering antenna has been installed on the LHD,²¹⁾ which can spatially scan the ECE/EBE signal around the mode conversion window, and the radial profile of radiation over the full minor radius of the LHD can be scanned during one discharge.

In this study, we developed a calibration method for a fast-steering antenna for investigating the mode conversion window used in EBW heating. The precise calibration was carried out in under-dense plasma using both the ECE measurement including an oblique angle to the magnetic field (oblique ECE) and ray-tracing calculations by integrating the local electron temperature along the calculated ray path following the solution of the radiation transport equation.²²⁾ This calculation can include the multi-reflected background ECE in optically thin lines-of-sight. An oblique ECE can be used to obtain the electron distribution function both in energy and in physical space.^{23, 24)} And then, the mode converted EBE measurement was attempted by scanning near the expected mode conversion window in over-dense plasma.

This paper is composed of five sections. In section 2, the ECE/EBE detection system including the fast steering antenna and the ECE calculation method using ray-tracing are briefly described. In section 3, for calibration of the measurement system, results of the ECE measurement using a fast steering radiometer and comparison with the calculation in under-dense plasma are discussed. In section 4, initial results of the EBE measurement near the mode conversion window in over-dense plasma are discussed. The summary of this paper is provided in section 5.

*E-mail: goto.yuki@k.mbox.nagoya-u.ac.jp

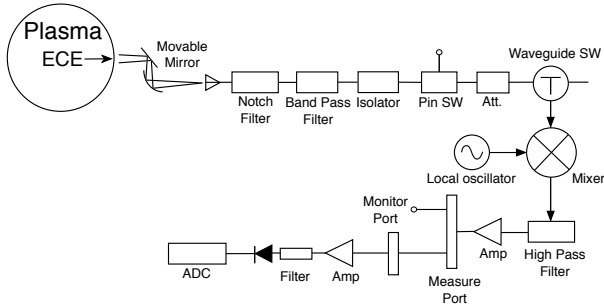


Fig. 1. ECE detection system: This antenna of the radiometer can be steered during the discharge to obtain the spatial distribution of the radiation.

2. ECE Detection System and ECE Calculation

LHD is a helical type fusion experiment device. The magnetic field structure which gives good confinement of the plasma is generated by two superconducting helical coils and three pairs of superconducting poloidal coils. The plasma poloidal cross section is almost elliptical and rotates 5 times to complete the one turn torus (toroidal period number: $n = 10$). In the experiment described in this paper, the magnetic axis and the field strength were set at 3.65 m and 2.712 T in the under-dense case.

2.1 ECE/EBE Detection System

The ECE/EBE detection system discussed here is the CTS (Collective Thomson Scattering) receiver system.^{21,25)} Because the CTS measurement requires a high S/N ratio, a high power gyrotron is used as a probe beam source. This system is furnished with a high sensitivity receiver to receive the weakly scattered signal. This receiver is composed of a heterodyne mixer, IF amplifiers, and filter banks that enable the detection of the ECE with 74-80 GHz as the IF frequency with 50-200 MHz. Fig.1 shows the schematic of the ECE/EBE measurement system used for this experiment. This system is installed on a low loss transmission line that is connected to a steerable mirror at a lower port (1.5L port) on the LHD. The upgrade of the steering speed of this mirror antenna system played an important role in the experiments described in this paper.

2.2 ECE Calculation Flow and Theory

In the LHD, the ray-tracing code LHDGauss has been developed to calculate the propagation and absorption of the EC-wave for the ECRH.^{26,27)} In this study, this ray-tracing code is used for calculating the local absorption rate along the ray path using magnetic field, electron temperature, and electron density. Since the local absorption rate can be determined along the ray path, it is possible to estimate the ECE for a given frequency as a solution of the radiation transfer equation discussed below. The absorption coefficient for oblique propagation discussed in²⁸⁾ is used in this calculation.

2.2.1 Ray-tracing In the weakly inhomogeneous magnetized plasma, the wave propagation can be treated so that the wave packet propagates in the direction and with the group velocity determined by the local dispersion relation. When the length scale of the electron density and magnetic field is large enough, as compared with

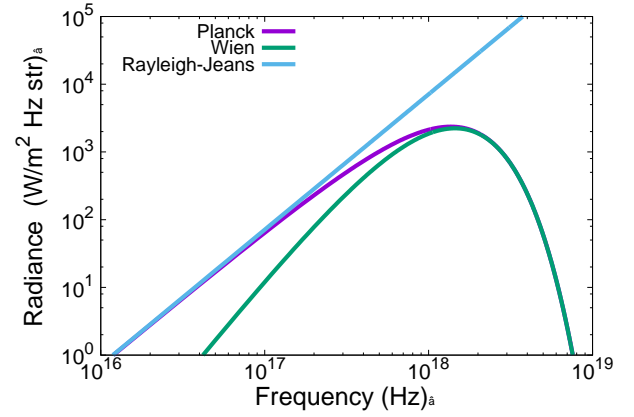


Fig. 2. Relationship of the radiance and the frequency when $kT = 2$ keV. The Rayleigh-Jeans law is comparable to the Planck's law below 10^{16} Hz at least in the range of from 0.5 keV to 3 keV.

the wavelength of the wave, it is possible to handle the wave propagation using geometrical optics. This is called a geometrical optics approximation. The method for obtaining the wave propagation path by tracking the wave packet is ray-tracing. In ray-tracing, the ray propagation in plasma is calculated from the vacuum side. Then, a local absorption coefficient along the ray path is calculated up to the point where the injected beam is completely absorbed. On the other hand, ECE intensity observed from the vacuum (antenna) side is the sum of the emission from each position on the ray path. Since the ray should follow the same path for injection/receiving from/by the antenna, the ECE can be calculated by integrating over the ray path using the radiation transfer equation. Such estimated ECE is equivalent to a radiation temperature to be discussed below. The ray path of an electromagnetic wave in plasma can be determined by the ray equation below.

$$\frac{d\mathbf{r}}{ds} = \frac{\partial G}{\partial \mathbf{k}}, \quad \frac{d\mathbf{k}}{ds} = -\frac{\partial G}{\partial \mathbf{r}}, \quad \frac{dt}{ds} = -\frac{\partial G}{\partial \omega}, \quad (1)$$

where $G(\mathbf{k}, \mathbf{r}, \omega)$ is the dispersion relation of the wave, which is satisfied with $G(\mathbf{k}, \mathbf{r}, \omega) = 0$. $\mathbf{k}(s)$, $\mathbf{r}(s)$, and t are wavevector, position, and time, respectively. s is a path length along the ray. Eq.(1) is related to the six dimensional (three in real space and three in wave-number space) simultaneous first order differential equations and can be solved numerically with the Runge-Kutta method for a fixed frequency.

2.2.2 Radiation Temperature The radiation temperature is the temperature of the black body that emits a radiation intensity equivalent to the measured intensity. The radiation temperature of the media with inhomogeneous temperature and absorption is given as the solution of a radiation transfer equation below.^{29,30)}

$$\frac{dI_\omega(s)}{ds} = j_\omega(s) - \alpha_\omega(s)I_\omega(s) \quad (2)$$

where s is the path length along the ray path. $I_\omega(s)$, $j_\omega(s)$, and $\alpha_\omega(s)$ are the radiance, radiation coefficient, and absorption coefficient, respectively. In order to solve this equation, it is necessary to know the relationship

between the radiance and the temperature. As follows, the Rayleigh-Jeans law gives the relationship between the radiance and the temperature.

$$B_0(s) = \frac{\omega^2}{2\pi^2 c^2} k_B T(s) \quad (3)$$

where $B_0(s)$, ω , c , and k_B are radiance, focused angular frequency, light speed, and Boltzmann's constant, respectively. Here the local radiance can be expressed using $j_\omega(s)$ and $\alpha_\omega(s)$ as $B_0(s) = \frac{j_\omega(s)}{\alpha_\omega(s)}$. This relation is Kirchhoff's radiation law. Although Planck's law and Wien's law also give the relationship between the radiance and the temperature, the Rayleigh-Jeans law is sufficiently accurate below 10^{16} Hz when assuming the electron temperature of 2 keV (Fig.2). Therefore, the radiation temperature $T_{\text{rad},\omega}(s)$ can be expressed in integral form as the general solution of eq.(2),

$$T_{\text{rad},\omega}(s) = \int T_e(s') e^{-\int_{s'}^s \alpha_\omega(s'') ds''} \alpha_\omega(s') ds' \quad (4)$$

where $T_e(s)$ is local electron temperature on the ray path. Here, $\tau(s') = \int_{s'}^s \alpha_\omega(s'') ds''$ is defined as an optical thickness. In the optically thick case, the radiation temperature corresponds to electron temperature on the resonance layer for focused frequency. On the other hand, in the optically thin case, various information from sources other than the resonance layer, which is being focused upon here, is dominant. Thus, radiation temperature does not represent the temperature at the resonance layer. In conclusion, when the ray path of the ECE can be determined by ray-tracing, we can calculate the radiation temperature as an integration of electron temperature along the ray path (eq.(4)).

3. Results of the ECE Measurement and the ECE Calculation

The ECE measurement and the ECE calculation were carried out on the under-dense plasma around 77 GHz. The under-dense experiments were performed to assess the validity of the calculations and the calibration of the measurement system. In the next section, we will discuss the EBE measurement near the mode conversion window by using the calibrated fast steering antenna.

Fig.3 shows the spatial distribution of the electron density and the electron temperature with several times when the stable plasma were sustained. The under-dense plasma has a line average electron density $n_e = 1.5 \times 10^{19} \text{ m}^{-3}$ and center electron temperature $T_e = 3 \text{ keV}$, and is sustained by ECRH and Ion Cyclotron Range of Frequency (ICRF) for about 30 sec. These figures show that the electron density and the temperature are not changed with time when the stable plasma was sustained. These parameters were measured by Thomson scattering with 17 mm of the spatial resolution and 30 Hz of the time resolution. The spatial resolution value is indicated on the major radius. But the effective radius is used to represent the plasma radius in this paper. The amount of helium gas-puffing is adjusted to keep the density constant. Fig.4 shows the ray path at several time slices when the stable plasma was sustained. Here, these slices show a cross section parallel to the injection plane

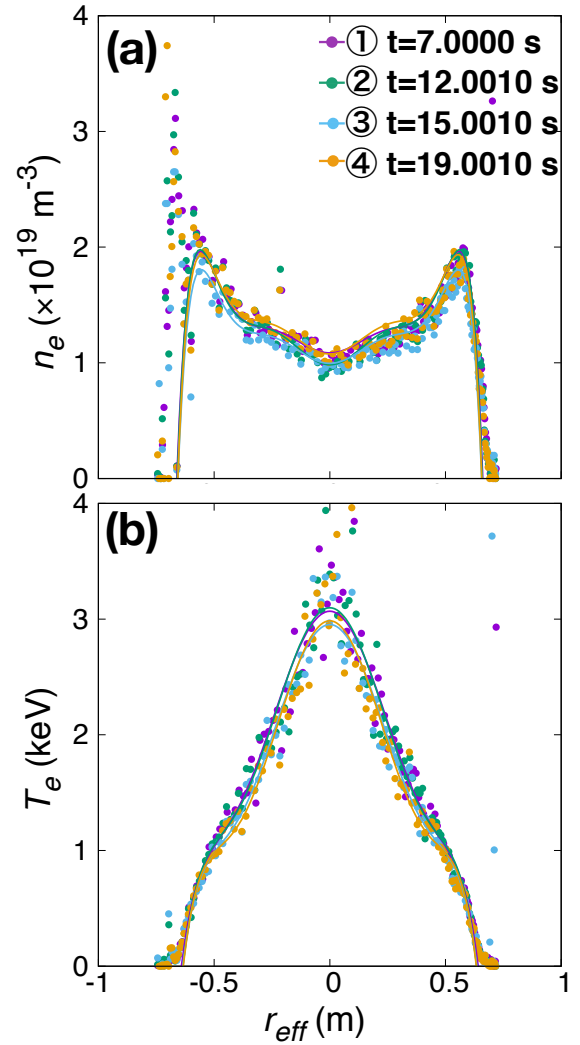


Fig. 3. (a): Spatial distribution of the electron density with several times. Horizontal axis means the effective radius. The electron density has no time changes, and is maintained under the cut-off density for 77 GHz. (b): Spatial distribution of the electron temperature with several times. Horizontal axis means the effective radius. The electron temperature has no time change. The dots indicate the measured data and the solid lines indicate the polynomial fitting curve.

including the final arrival point. Fig.5 shows the comparison of the time variations of the measured ECE signal, the calculated ECE by eq.(4) with using the plasma parameters as shown in Fig.6, the optical thickness, and the antenna scanning line of sight in the same ray path scanning as shown in Fig.4. In the experiment, although the ray path does not pass through the resonance layer within the plasma region during the period about 9 to 13 sec., a certain constant level signal is measured. This indicates that the multi-reflection effect dominates in the optically thin ray path. The multi-reflection effects between the wall and the plasma produce a nearly isotropic microwave background. However, the ECE calculation using eq.(4) does not include such background radiation. In order to take this effect into account, a background radiation temperature is assumed such that the temperature is equivalent to β times of the central electron temperature. That is,

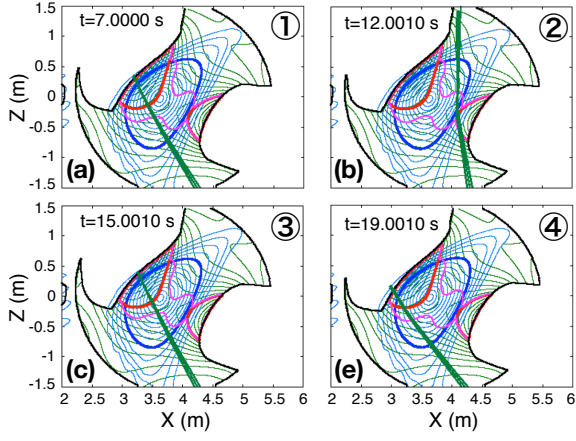


Fig. 4. (a), (b), (c), and (d) show the slices at the incident beam plane at each time when under-dense plasma is sustained. The bold green and blue lines are ray path and a99, the red and magenta lines are 77 GHz resonance layer and UHR layer. The a99 is defined by the effective radius of the plasma in which 99% of the plasma energy is stored.

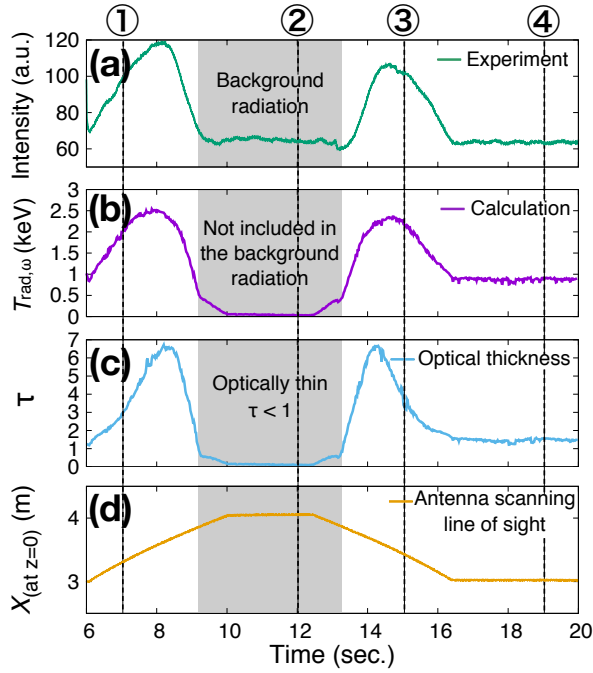


Fig. 5. Comparison of the time variation when the fast steering antenna is scanned spatially as shown in Fig.4. (a), (b), (c), and (d) show the measured ECE at 77.2 GHz, the calculated radiation temperature, the optical thickness, and the antenna scanning line of sight. The definition of the line of sight for steering position is based on $z = 0$.

$$T_b(t) = \beta T_0(t) \quad (5)$$

where β is the background radiation factor and $T_0(t)$ is the electron temperature at the plasma minor radius $r = 0$ in each time slice. Calibration is carried out by adding $T_b e^{-\tau}$ to eq.(4). Here the τ is the optical thickness when the ray arrives at the wall from the antenna. The calibration equation is given below

$$I = \frac{1}{C} \left(T_b e^{-\tau} + \int T_e(s') e^{-\int_{s'}^s \alpha_\omega(s'') ds''} \alpha_\omega(s') ds' \right), \quad (6)$$

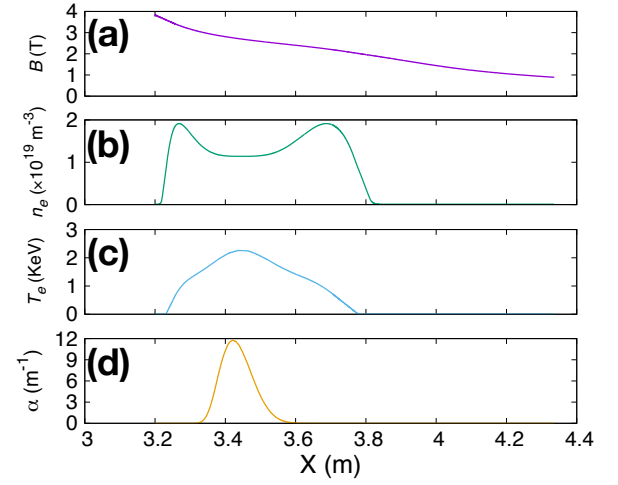


Fig. 6. Plasma parameters at the time on Fig.4(a) for #131000 for X axis with respect to ray path. (a), (b), (c), and (d) show the magnetic field strength, the electron density, the electron temperature, and the absorption rate, respectively.

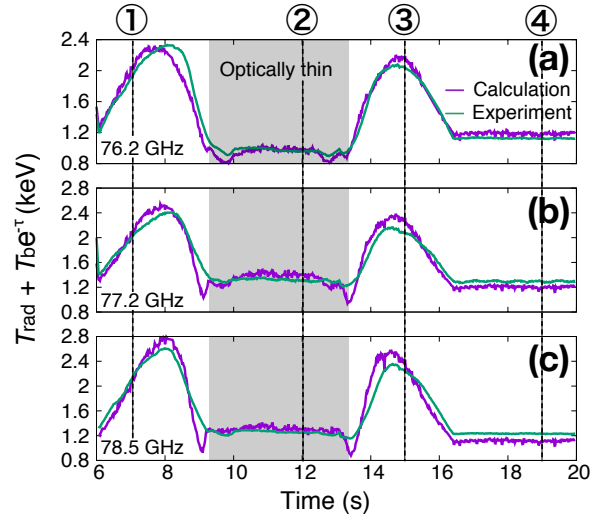


Fig. 7. Comparison of the time variation of the calibrated measured ECE and calculated ECE included the background radiation. (a), (b), and (c) show the results at 76.2, 77.2, and 78.5 GHz, respectively.

where I and C are the calculated radiation temperature including background radiation and the calibration factor. This equation means that the radiation intensity from optically thin ray path is dominated by the background radiation. On the other hand, the background radiation becomes negligibly small when the optical thickness is large because the background radiation is almost completely absorbed, and the observed intensity is dominated by emission from the optically thick ray path. The local absorption rate is a function of B and local plasma parameters such as T_e , n_e , and propagation direction relative to the magnetic field. Fig.6 shows the plasma parameters at the time on Fig.4(a) for #131000 for X axis with respect to ray path. The plasma parameters T_e and n_e required in the ECE calculation are obtained from the Thomson scattering measurement at each time slice mapped on the flux surfaces. The calibration factor C

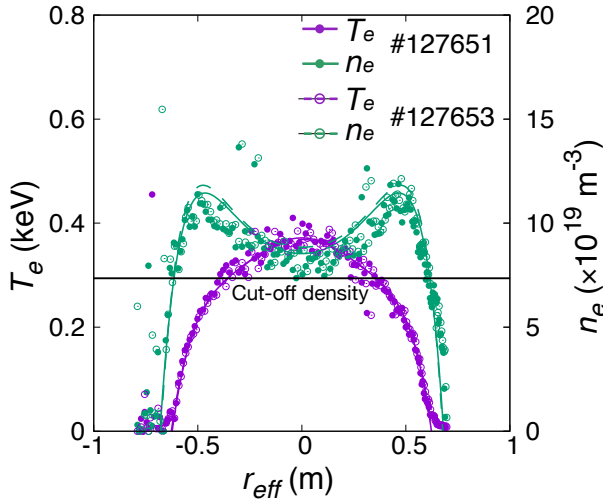


Fig. 8. Spatial distribution of the electron density and the electron temperature for the shots #127651 and #127653 at 5.0 sec. Horizontal axis means the effective radius.

and the background radiation factor β in the eq.(6) are calculated by least-squares fitting. The calculated $\beta_{76.2}$, $\beta_{77.2}$, and $\beta_{78.5}$ are 0.4159, 0.4867, and 0.4203, respectively. Fig.7 shows the time variation of the calibrated ECE and the calculated radiation temperature taking the background radiation into account. It was possible to precisely calibrate the measured signal, including the optically thin period during about 9 to 13 sec., by considering the background radiation. Also, the multi-ray calculation was carried out in order to take the finite beam size effect into account. This effect becomes particularly important when the beam passes through near the boundary of the resonance layer. This calibration method that we developed here can be applied to a measurement system, which has a line-of-sight with an optical thickness which varied spatially.

4. Initial Results of the EBE Measurement near the Mode Conversion Window

In the over-dense case, the He plasma with high reproducibility and long duration was generated and sustained by the five neutral beam injections (NBI). He gas-puffing was adjusted to maintain the electron density above the cut-off density and to stay constant during scanning period. Fig.8 shows the spatial distribution of the electron density and the electron temperature for the shots #127651 and #127653 at 5.0 sec. The over-dense state was produced when the stable plasma was sustained.

Fig.9(a), (b), and (c) show the time variation of the measured radiation during fast scanning. The scanning path could not be set on the predicted mode conversion window with higher efficiency because of the hardware restriction of the steering. The fast scanning was carried out from 4.7 to 5.7 sec. for discharge #127651 and from 5.1 to 6.0 sec. for discharge #127653. The tendency with increase of the measured radiation near this region is confirmed experimentally while almost over-dense plasma is sustained. When the antenna scan time is shifted by 0.4 sec. for the two shots (as shown in Fig.9(f)),

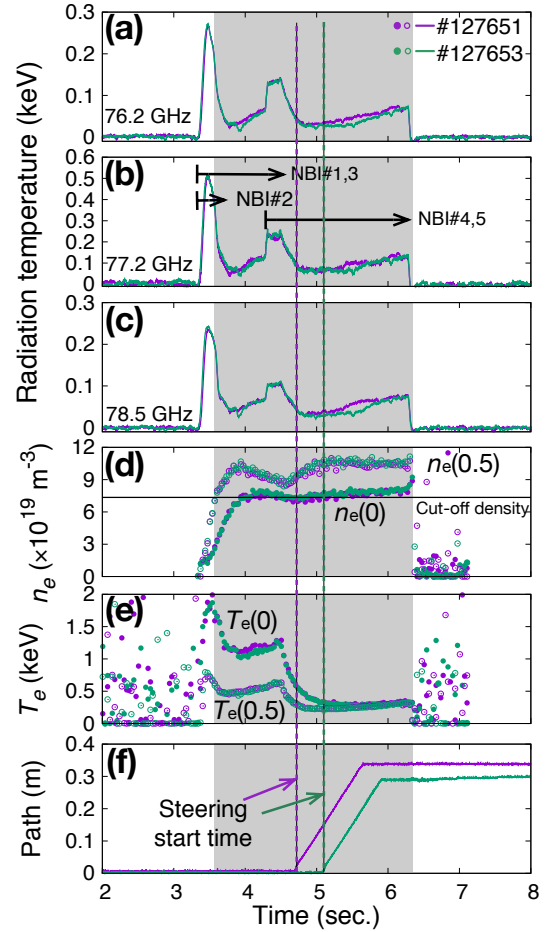


Fig. 9. (a), (b), (c): Time variation of the measured radiation at each frequency for the shots #127651 and #127653. (d), (e): Time variation of the electron density and the temperature at the effective radius $r_{eff} = 0$ m and 0.5 m. (f): Time variation of the antenna scanning line of sight. The tendency with increase of the measured radiation around the mode conversion window is confirmed experimentally while almost over-dense plasma is sustained. When the antenna scan time is shifted by 0.4 s for the two shots, the increase of the measured radiation is shifted correspondingly.

the increase of the measured radiation is shifted correspondingly. While the electron temperature and the density measured by Thomson scattering for both shots are maintained identical (Fig.9(d) and (e)), it is confirmed that this change of the radiation is not due to the time variation, but is the spatial structure of the radiation. The path written on the vertical axis in Fig.9(f) is defined as shown in Fig.10, which is the intersection with the line-of-sight at the mid-plane. In addition, Fig.11 shows the spatial distribution of the measured radiation for each frequency. This figure represents the radiation intensity on the path defined as shown in Fig.10. Although the increase of the measured radiation shifted correspondingly when the antenna scanning time is shifted for the two shots in Fig.9(a), (b), and (c), the tendency of the measured radiations are overlapped when the horizontal axis is the path. In other words, it can be seen that this radiation has spatial distribution.

Also, the ECE calculation using ray-tracing in the over-dense state was carried out in order to distinguish

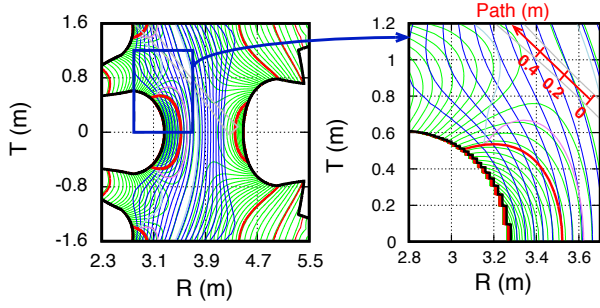


Fig. 10. Definition of the path for the line-of-sight. The line-of-sight of the antenna is defined by coordinate on the mid-plane (R - T plane at $z = 0$) of the LHD plasma.

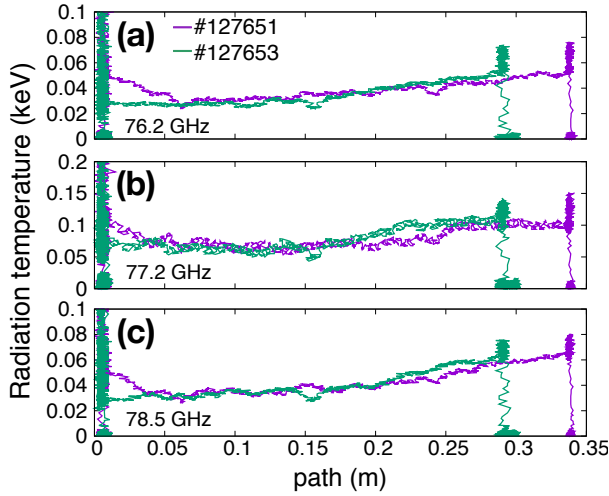


Fig. 11. (a), (b), (c): Spatial distribution of the measured radiation at each frequency for the shots #127651 and #127653. The tendency of the measured radiations are overlapped when the horizontal axis is the path.

EBE from ECE. The calculation results of the ECE are negligibly small, and the order is 10^{-6} keV. This emission source is located only near the wall and clearly outside of the plasma cut-off (Fig.12). Fig.12 shows the trajectory of the rays in the over-dense plasma. Here, Fig.12 bottom shows a horizontal cross section including the final arrival point. After the rays are reflected at the plasma cut-off, it can be seen that the rays are propagating toward the vacuum chamber wall. Fig.13 shows the parameters such as magnetic field strength, electron temperature and electron density, and absorption coefficient for X axis with respect to the rays path. The plasma density and temperature are negligibly small because the resonance condition ($B = 2.75$ T for 77 GHz) is located only near the wall. This is the reason why the calculated ECE is negligibly small. Although there is an emission source of the ECE outside of the plasma cut-off, the increase in the measured radiation (Fig.9) cannot be explained as the ECE process when the over-dense plasma is sustained. This measured radiation and the tendency to increase during antenna scan can be explained by the EBE instead of the ECE. The measured radiation is originated from EBW inside of the plasma cut-off and is emitted from through the mode conversion window.

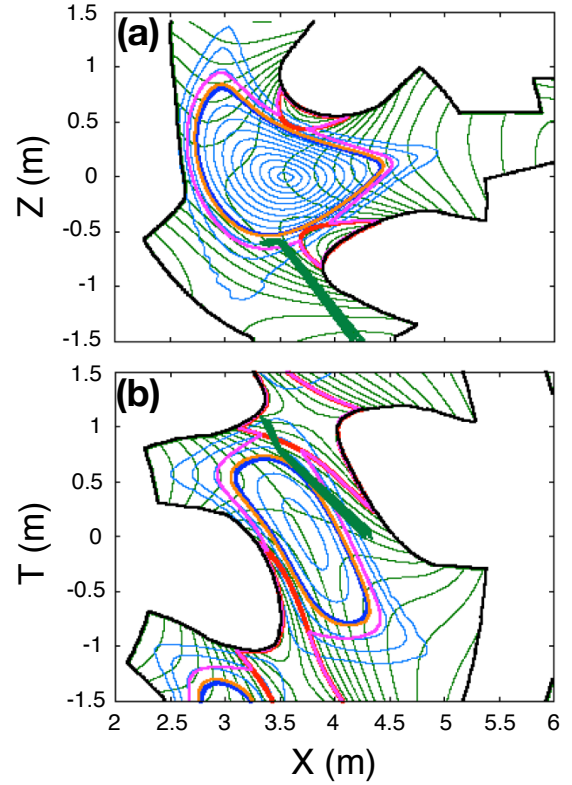


Fig. 12. Beam trajectories at 5.6 sec for #127651 when over-dense plasma is sustained. (a): Slices at the incident beams plane projected on the z direction. (b): Slices at the incident beams plane projected on the T direction. The orange line is plasma cut-off. Incident beams pass through near the resonance layer. After that, the reflected beams propagate toward the wall.

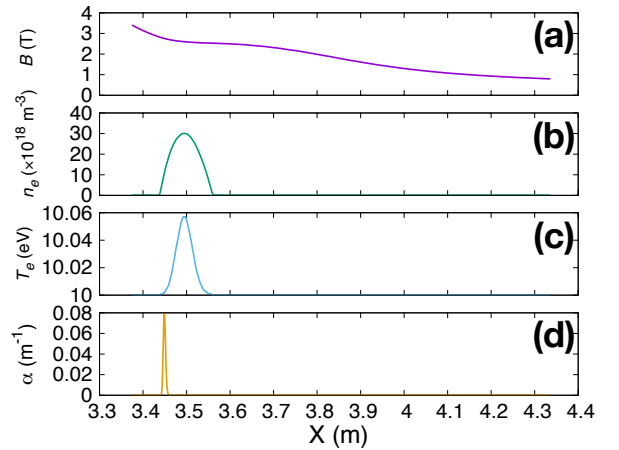


Fig. 13. Plasma parameters at 5.6 sec. for #127651 for X axis with respect to ray path. (a), (b), (c), and (d) show the magnetic field strength, the electron density, the electron temperature, and the absorption rate, respectively.

5. Summary

In the LHD, the ECE measurement using a fast steering antenna and the ECE calculation using ray-tracing were carried out. An experimental ECE measurement in under-dense plasma was carried out in order to calibrate the measurement system for investigating of the mode

conversion window in the over-dense plasma. Calibration was carried out by including the multi-reflected background radiation in the optically thin line of sight. Therefore we could establish the general calibration method of a fast steering antenna. Also, this study is helpful for calibration of the CTS measurement system. The space non-uniformity of the measured radiation is confirmed experimentally when the over-dense plasma is sustained. The ECE calculation using ray-tracing in the over-dense state was carried out in order to distinguish the ECE from the mode converted EBE. This increase of the measured radiation in the over-dense experiment cannot be explained as the ECE. This is because there is no emission source for the ECE which can explain the increase of the radiation outside of the plasma cut-off. Therefore, the measured radiation in over-dense state is the EBE via the inverse mode conversion mechanism that originates from thermally excited EBW in the plasma core region.

Acknowledgments

The authors would like to express their thanks to technical staff for performing the LHD experiments. This research was supported by the National Institutes for Fusion Science (NIFS) code of NIFSULRR701 and NIFSULR033.

References

- 1) I. B. Bernstein, Phys. Rev., **109**, 10 (1958).
- 2) T. H. Stix, "Waves in Plasmas," Springer, (1992).
- 3) S. J. Diem, D. L. Green, R. W. Harvey, and Y. V. Petrov, Phys. Plasmas **25**, 072124 (2018).
- 4) A. K. Ram and S. D. Schultz, Phys. of Plasmas **7**, 4084 (2000).
- 5) H. P. Laqua, Plasma Phys. Control. Fusion, **49**, R1 (2007).
- 6) H. P. Laqua, H. Maassberg, F. Volpe, W7-AS Team and ECRH-Group, Nucl. Fusion, **47**, 11, 1324–1328 (2003).
- 7) H. P. Laqua, V. Erckmann, H. J. Hartfuß, and H. Laqua (W7-AS Team ECRH Group), Phys. Rev. Lett. **78**, 3467 (1997).
- 8) V. Shevchenko, Y. Baranov, M. O'Brien, and A. Saveliev, Phys. Rev. Lett., **89**, 265005 (2002).
- 9) V. Shevchenko, T. Bigelow, J. B. Caughman, S. Diem, J. Mailloux, M. R. O'Brien, M. Peng, A. N. Saveliev, Y. Takase, H. Tanaka, and G. Taylor, EPJ Web Conf., **87**, (2015)
- 10) T. Maekawa, T. Kobayashi, S. Yamaguchi, K. Yoshinaga, H. Igami, M. Uchida, H. Tanaka, M. Asakawa, and Y. Terumichi, Phys. Rev. Lett. **86**, 3783 (2001).
- 11) Y. Yoshimura, K. Nagasaki, T. Akiyama, M. Isobe, A. Shimuzu, C. Suzuki, C. Takahashi, K. Nagaoka, S. Nishimura, T. Minami, K. Matsuoka, S. Okamura, CHS group, S. Kubo, T. Shimozuma, H. Igami, T. Notake, and T. Mutoh, Plasma Fusion Res., **1**, 029 (2006).
- 12) F. R. Hansen, J. P. Lynov, and P. Michelsen, Plasma Phys. Control. Fusion, **27**, 10, 1077–1100 (1985).
- 13) J. Preinhaelter and V. Kopecky, J. Plasma Phys., **10**, 1 (1973).
- 14) S.J. Diem, G. Taylor, J.B. Caughman, P.C. Efthimion, H. Kugel, B.P. LeBlanc, C.K. Phillips, J. Preinhaelter, S.A. Sabbagh, J. Urban, and J.B. Wilgen, Nucl. Fusion **49**, 095027 (2009).
- 15) J. Preinhaelter, J. Phys. B, **25**, 1, 39–50 (1975).
- 16) A. K. Ram, A. Bers, S. D. Schultz, and V. Fuchs, Phys. Plasmas, **3**, 5, 1976–1982, (1982).
- 17) K. G. Budden, "The Propagation of Radio Waves," Cambridge University Press, (1988).
- 18) V. Fuchs, A. K. Ram, S. D. Schultz, A. Bers, and C. N. Lashmore-Davies, Phys. Plasmas, **2**, 5, 1637–1647 (1995).
- 19) S. J. Diem, G. Taylor, J. B. Caughman, P. Efthimion, H. Kugel, B. P. LeBlanc, J. Preinhaelter, S. A. Sabbagh, J. Urban, and J. Wilgen, Rev. Sci. Instrum., **79**, 10F101 (2008).
- 20) H. P. Laqua, H. J. Hartfuß, and W7-AS Team, Phys. Rev. Lett. **81**, 2060 (1998).
- 21) K. Okada, M. Nishiura, S. Kubo, T. Shimozuma, Y. Yoshimura, H. Igami, H. Takahashi, K. Tanaka, S. Kobayashi, S. Ito, Y. Mizuno, and S. Ogasawara, Rev. Sci. Instrum., **85**, 11E811 (2014).
- 22) N. B. Marushchenko, V. Erckmann, H. J. Hartfuss, M. Hirsch, H. P. Laqua, H. Maassberg, and Y. Turkin, Plasma Fusion Res., **2**, S1129, 1–5 (2007).
- 23) S. Preische, L. Porte, S. Alberti, P. Blanchard, A. Fasoli, and T. P. Goodman, Rev. Sci. Instrum., **68**, 409 (1997).
- 24) T.P. Goodman, V. S. Ushintsev, I. Klimanov, A. Mueck, O. Sauter, and C. Schlatter, Fusion Sci. Technol., **53**, 1 (2008).
- 25) M. Nishiura, S. Kubo, K. Tanaka, R. Seki, S. Ogasawara, T. Shimozuma, K. Okada, S. Kobayashi, T. Mutoh, and K. Kawahata, Nucl. Fusion, **54**, 023006 (2014).
- 26) S. Kubo, H. Idei, T. Shimozuma, Y. Yoshimura, T. Notake, K. Ohkubo, S. Inagaki, Y. Nagayama, K. Narihara, I. Yamada, S. Muto, S. Morita, and LHD Experimental Group, AIP Conference Proceedings **669**, 187 (2003).
- 27) T. I. Tsujimura, S. Kubo, H. Takahashi, R. Makino, R. Seki, Y. Yoshimura, H. Igami, T. Shimozuma, K. Ida, C. Suzuki, M. Emoto, M. Yokoyama, T. Kobayashi, C. Moon, K. Nagaoka, M. Osakabe, S. Kobayashi, S. Ito, Y. Mizuno, K. Okada, A. Ejiri, T. Mutoh and the LHD Experiment Group, Nucl. Fusion, **55**, 123019 (2015).
- 28) M. Bornatici, R. Cano, O. D. Barbieri, and F. Engelmann, Nucl. Fusion, **23**, 9, 1153–1257 (1983).
- 29) G. Bekefi, "Radiation Processes in Plasmas," Wiley, (1966).
- 30) W. P. Allis, S. J. Buchsbaum, and A. Bers, "Waves in Anisotropic Plasmas," The MIT Press, (2003).